Elasto-Plastic Design of Ultrathin Interlayer for Enhancing Strain Tolerance of Flexible Electronics

Hong Hu[1], *Xuyun Guo*[2], *Yaokang Zhang*[1], *Zijian Chen*[1], *Lei Wang*[1], *Yuan Gao*[1], *Ziran Wang*[1], *Yuqi Zhang*[1], *Wenshuo Wang*[1], *Mingming Rong*[1], *Guoqiang Liu*[1], *Qiyao Huang*[1], *Ye Zhu*[2], *Zijian Zheng*[1,3,4,5]*

[1]Laboratory for Advanced Interfacial Materials and Devices, School of Fashion and Textiles, The Hong Kong Polytechnic University, Hong Kong SAR, China

[2]Department of Applied Physics, The Hong Kong Polytechnic University, Hong Kong SAR, China

[3]Department of Applied Biology and Chemical Technology, Faculty of Science, The Hong Kong Polytechnic University, Hong Kong SAR, China

[4]Research Institute for Intelligent Wearable Systems (RI-IWEAR), The Hong Kong Polytechnic University, Hong Kong SAR, China

[5]Research Institute for Smart Energy (RISE), The Hong Kong Polytechnic University, Hong Kong SAR, China

Keywords: interlayer, yield strain, Young's modulus, strain tolerance, flexible electronics

Abstract

The ability to tolerate large strains during various degrees of deformation is a core issue in the development of flexible electronics. Commonly used strategies nowadays to enhance the strain tolerance of thin film devices focus on the optimization of the device architecture and the increase of bonding at the materials interface. In this paper, we propose a strategy, namely elasto-plastic design of ultrathin interlayer, to boost the strain tolerance of flexible electronics. We demonstrate that insertion of an ultrathin, stiff (high Young's modulus) and elastic (high yield strain) interlayer between an upper rigid film/device and a soft substrate, regardless of the substrate thickness or the interfacial bonding, can significantly reduce the actual strain applied on the film/device when the substrate is bent. Being independent to existing strategies, the elasto-plastic design strategy offers an effective method to enhance the device flexibility without redesigning the device structure or altering the materials interface.

Introduction

The rapid development of flexible electronics in the past decade has enabled a wide variety of emerging applications ranging from soft human-machine interface[1], electronic skin[2-4], energy[5, 6], and implantable bioelectronics[7], to flexible and stretchable displays[8-10], and smart wearables[11-13]. Because flexible devices are highly deformable, materials in these devices experience different degrees of tensile strains during the bending, stretching, compressing, and twisting of the devices[14, 15]. While polymeric substrates used for fabricating the devices are often compliant enough, other materials such as metals, inorganic semiconductors, and ceramics are too brittle to withstand the tensile strains. Unfortunately, despite the intensive effort on developing various types of soft materials in the past decades, these brittle materials are still indispensable in most device applications[16-18]. For example, metal is widely used as the electrode, interconnect, lead, and contact in flexible electronics due to the intrinsically high conductivity and the excellent compatibility with conventional manufacturing process[14]. However, governed by the plastic nature, metal films usually fracture at a small tensile strain (~1%)[8, 19], which is much smaller than most strains experienced during flexing of the device (>3%) and hence causes significant performance lost and device failure (Figure 1a)[20].

To date, there are two major principles that guide the materials design and device fabrication to minimize the actual tensile strains applied on those rigid materials, so as to improve the flexibility of the thin film devices. The first principle is fabricating devices on ultrathin substrates (Figure 1b)[21]. It is known that the largest tensile strain (ε) of a bent thin film device is approximately equivalent to $\varepsilon=T/2R$, where T is the thickness of the device and R is the bending radius[22]. Therefore, in order to bend the device with a smaller R, T should be as small as possible. Following this principle, ultrathin materials of several tens to several hundreds of nm are typically deposited on plastic substrates of several μm to fabricate ultrathin flexible electronics. In combination with additional structural design including in-plane serpentine[23], out-of-plane buckle[24], and strain-relief structure[25-27], this strategy can be extended to a high stretchability of the device.

The second principle to realize high flexibility is increasing the interfacial adhesion between the rigid materials and the flexible substrate (Figure 1c)[19, 28, 29]. This is because an interface of high binding energy can suppress the strain localization of the upper-layered rigid material during flexing, which is the major course of fracture of the rigid film at a tensile status[29]. The interfacial adhesion is often enhanced by surface treatments of the substrate via ultraviolet (UV) ozone[30] or oxygen plasma[31], or by introducing an adhesion layer (e.g., Cr[32]) of several nm thick prior to the deposition of the rigid material. It should be noted that these two major principles are independent to each other. Therefore, one can apply both strategies simultaneously to significantly enhance the flexibility of a thin film device[3, 23, 33].

In this paper, we report a third independent principle, which is named the elasto-plastic design of interlayer materials, to enhance the strain tolerance and hence the flexibility of the device. The key idea of this elasto-plastic design is to insert an ultrathin (<100 nm) layer of materials (the interlayer) between the rigid material and the underlying flexible substrate (Figure 1d). We show that an interlayer simultaneously possessing a high Young's modulus (E, representing stiffness) and a high yield strain (ε_Y, representing the elastic region) can significantly reduce the actual strain applied on the rigid materials at a tensile status. More importantly, we demonstrate that the elasto-plastic design is independent to the existing substrate thinning or the interfacial adhesion strategies discussed above. Therefore, one can apply the elasto-plastic design, in additional to the existing principles, to further enhance the strain tolerance of flexible devices.

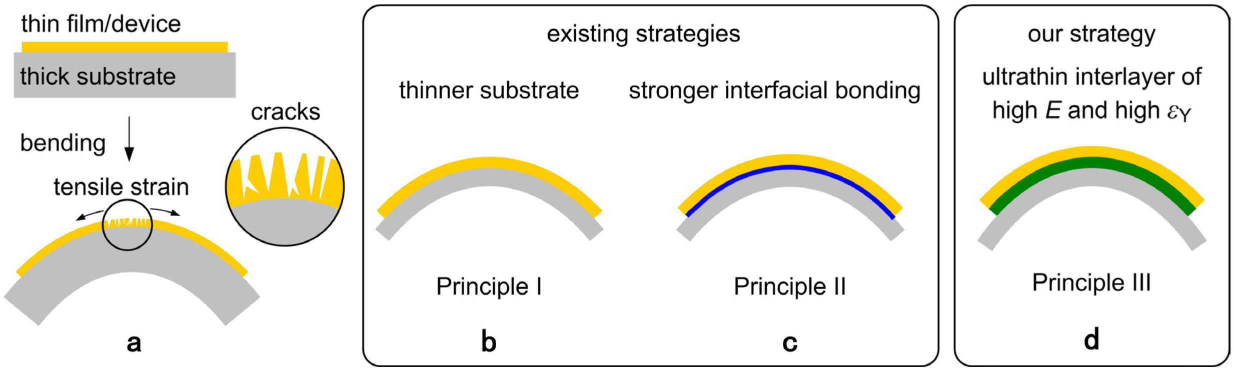

Figure 1. Schematic comparison of strategies to enhance the flexibility of electronic devices. a) A rigid thin film or device, which is deposited on a thick soft substrate, can easily crack when the substrate is bent because the tensile strain (ε) applied on the rigid film exceeds the yield strain (ε_Y) of the material. b) Thinning of the substrate can effectively reduce the tensile strain, according

to the equation $\varepsilon=T/2R$, where T is the thickness and R is the bending radius. c) Increasing the interfacial binding energy between the rigid film and the substrate is a second strategy to enhance the flexibility of the device. Strong interfacial bonding can suppress the strain localization of the upper-layer rigid material, and thus enhance the strain tolerance. d) The elasto-plastic design of ultrathin interlayer is proposed as the third strategy to enhance the flexibility of the device. An ultrathin interlayer (~100 nm) simultaneously possessing high Young's modulus and high yield strain can reduce the actual strain applied on the rigid material/device when the substrate is bent. The principle is independent to and compatible with the existing strategies shown in b) and c).

Results

To illustrate the elastic-plastic interlayer theory, we first simulated the bending behavior of a tri-layer structure (Figure 2a) consisting of an upper rigid film, an ultrathin interlayer, and an underlying compliant substrate using finite element analysis (FEA). We studied the tensile strain of the upper film of the tri-layer structure as a function of the E and ε_Y of the interlayer, and then normalized by the tensile strain of the same upper film of a bi-layer structure without the interlayer (Figure 2b). As such, the normalized tensile strain, $\bar{\varepsilon}$, can describe the strain tolerance of the tri-layer structure using different interlayer materials, where a smaller $\bar{\varepsilon}$ represents a better strain tolerance (details of the simulation are described in Materials and Methods).

As shown in Figure 2c, a 100 nm thick interlayer of low E or low ε_Y (bottom left corner of the figure) resulted in $\bar{\varepsilon}>1$, i.e., an ultrathin interlayer that is either too soft or too brittle will accelerate the yield of the upper rigid film, which leads to easy cracking of the film during flexing. $\bar{\varepsilon}$ decreased when either E or ε_Y increased. When the interlayer possessed both high E and high ε_Y

(upper right corner of the figure), $\bar{\varepsilon}$ reached minimum, i.e., the insertion of a stiff and elastic interlayer is an effective approach to reducing the actual applied strain of the upper rigid film during bending. Note that, either of E or ε_Y can separately influence the deformation behavior of the upper film (Supplementary Figures S1 and S2), but has different weights in determining $\bar{\varepsilon}$ according to the gradient field of $\nabla\bar{\varepsilon}$ (Supplementary Figure S3).

We further studied the dependences of $\bar{\varepsilon}$ on the thickness of interlayer (0 to 500 nm) and the yield strain of upper film (0 to 10%). A stiff and elastic interlayer (E=400 GPa and ε_Y=4%, indicated with * in Figure 2c) was studied against a soft and brittle interlayer (E=3 GPa and ε_Y=1%, indicated with ** in Figure 2c). We found that, regardless of the interlayer thickness or the yield strain of the upper film, the stiff and elastic interlayer always led to a much lower $\bar{\varepsilon}$ than the soft and brittle one (Figure 2d and Figure 2e). This result implies that the elasto-plastic design principle of the interlayer is a versatile materials strategy independent to the structure thickness and the material property of upper film.

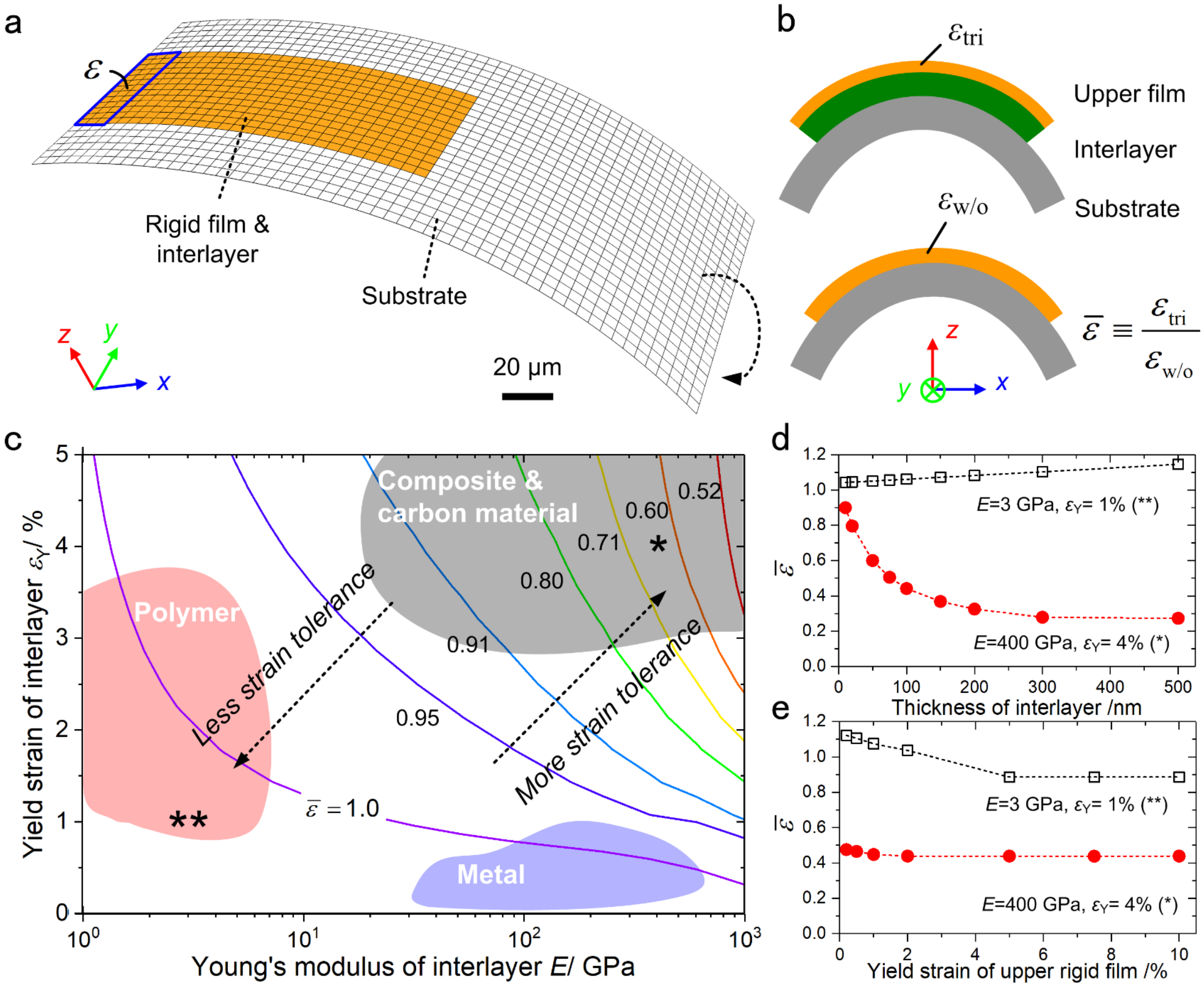

Figure 2. Finite element analysis (FEA) of the elasto-plastic design of ultrathin interlayer for enhancing the strain tolerance of flexible electronics. a) Geometrical model of FEA to study the typical bending behavior of a thin film device on a compliant substrate. The averaged tensile strain ε applied at the center of the small region of the rigid film (blue rectangle) is measured when the substrate is bent. b) Schematic illustration showing the calculation of normalized strain $\bar{\varepsilon}$. The tensile strains of tri-layer structure with the interlayer (ε_{tri}) and bilayer structure without the interlayer ($\varepsilon_{\text{w/o}}$) are simulated with FEA simulations. $\bar{\varepsilon}$ is defined as the ratio between ε_{tri} and $\varepsilon_{\text{w/o}}$. c) Contour plot showing $\bar{\varepsilon}$ as a two-variable function of the Young's modulus E and yield strain ε_Y of the interlayer. Smaller $\bar{\varepsilon}$ appears at the top-right corner of the figure, meaning that interlayer

with higher E and ε_Y provides better strain tolerance. d) and e) Dependences of $\bar{\varepsilon}$ on thickness of interlayer and yield strain of upper film, respectively. Regardless of the thickness variation on the interlayer or the yield strain of the upper filminterlayer materials possessing high E and ε_Y (note with * in c) always result in smaller $\bar{\varepsilon}$, i.e., better strain tolerance, than the interlayer posssessing low E and ε_Y (note with ** in c).

To verify the elasto-plastic design principle, we deposited ultrathin layers of Cu (~40 nm) on thin polyimide (PI) substrates (~5,000 nm) with or without an ultrathin interlayer. Table 1 summarizes the properties of the deposited materials. Sample i (Cu/PI) serves as a reference and its $\bar{\varepsilon}$ is 1.00. Polymethyl methacrylate (PMMA) and Cr were chosen as interlayer for Sample ii (Cu/PMMA/PI) and Sample iii (Cu/Cr/PI) respectively, because they are widely used as interfacial materials in many electronic devices yet exhibit significant difference in the elasto-plastic properties[34-39]. PMMA represents a soft (E=4.2±0.8 GPa) yet elastic interlayer (ε_Y=3.4 %), while Cr represents a stiff (E=265±15 GPa) yet brittle interlayer (ε_Y=0.9 %). The $\bar{\varepsilon}$ of Sample ii and Sample iii are 0.97 and 1.01, respectively.

A Cu-polymer nanocomposite interlayer, prepared by the polymer-assisted metal deposition (PAMD) method[40], was chosen as the interlayer of Sample iv (Cu/nanocomposite/PI). Figure 3a shows the cross-sectional structures of these samples. Note that the energy dispersive X-ray spectroscopy (EDS) mapping illustrated that the Cu nanoparticles were uniformly embedded in the polymer matrix in Sample iv. This is because the Cu nanoparticles were formed by *in situ* electroless deposition within the grafted polymer matrix in the PAMD process[41, 42]. Importantly, E and ε_Y of the nanocomposite interlayer were determined to be 39.2±2.04 GPa and 3.8%, respectively, indicating that the nanocomposite is a stiff and elastic interlayer (details of measurements and analysis can be found in Materials and Methods, Supplementary Note I, and in Supplementary Figures S4 and S5). As such, the $\bar{\varepsilon}$ of Sample iv is 0.89, showing that the nanocomposite interlayer falls in the desirable elasto-plastic regime of the FEA simulation results. Note also that, to highlight the role of the material property of the interlayer on the actual strain on the upper rigid film in deformation, which will be experimentally evaluated by the behaviors of crack and conductive resistance in the following section, the material property of the upper film is required to be identical among these samples. For this reason, the Cu in Samples i-iii were all deposited by the PAMD method, in which the thickness of the copolymer was strictly constrained in a geometrically negligible level (<5 nm) (Details can be found in Materials and Methods).

Table 1. Summary of some key information of the four samples under investigation

Label	Structure & material	Thickness (nm)	E (GPa)	ε_Y (%)	$\bar{\boldsymbol{\varepsilon}}$
Sample i	Cu/PI	40/5000	N/A	N/A	1.00
Sample ii	Cu/PMMA/PI	40/120/5000	4.2±0.8[34, 35]	3.4[36]	0.97
Sample iii	Cu/Cr/PI	40/120/5000	265±15[37, 38]	0.9[39]	1.01
Sample iv	Cu/nanocomposite/PI	40/130/5000	39.2±2.04	3.8	0.89

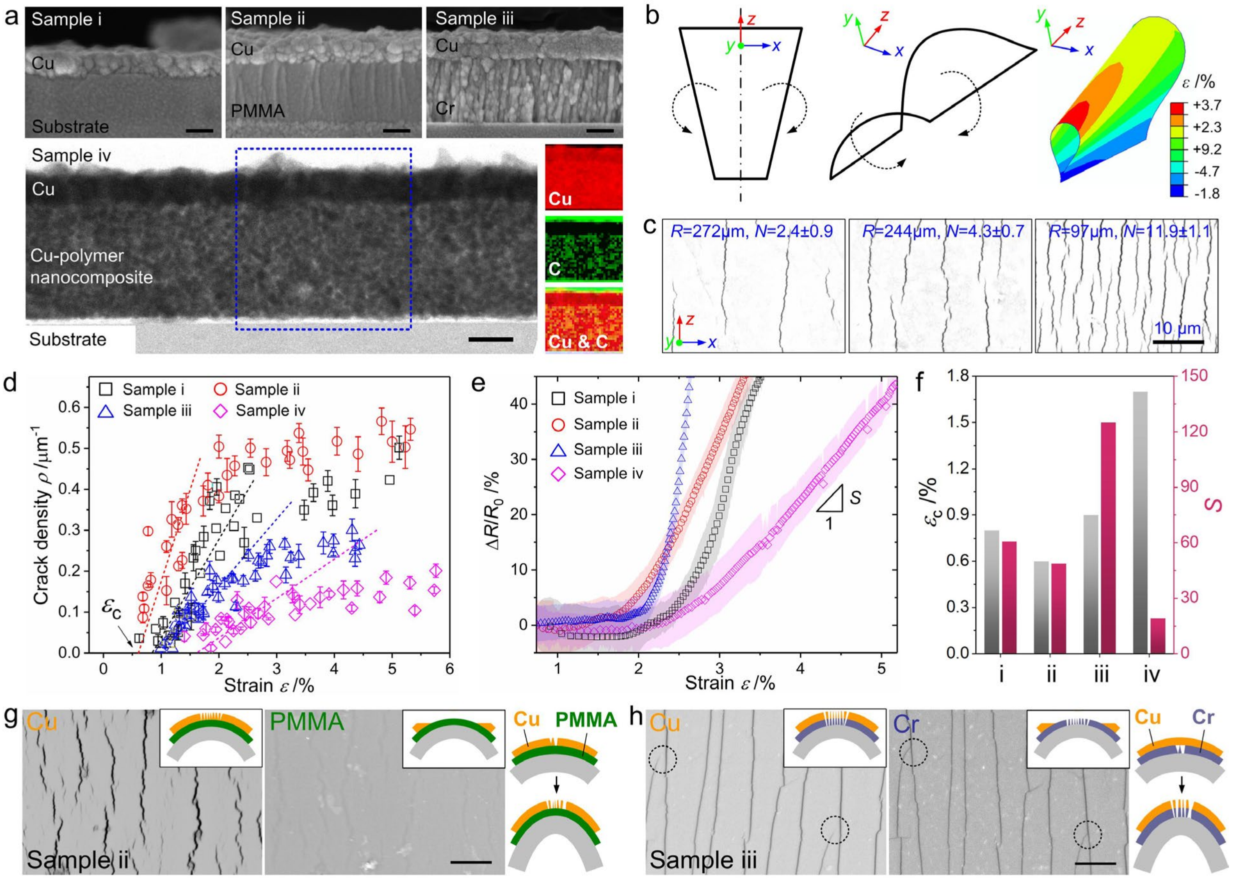

Figure 3. **Bending behaviors of Cu electrodes deposited on PI with different ultrathin interlayers**. a) Cross-sectional images of the Cu electrode without interlayer (Sample i), with PMMA interlayer (Sample ii), with Cr interlayer (Sample iii), and with a Cu-polymer nanocomposite interlayer (Sample iv). The scale bars are 50 nm. The elemental mappings showed the distributions of Cu and C in Sample iv. b) Schematic of the bending experiment that enables a continuously varied tensile strain *ε*. c) Representative SEM images of microcracks on the surface of Sample iv at locations of different bending radii. *N* is the crack number, and *R* is the bending radius calculated by the linear relation between *R* and *z* position (Supplementary Figure S6). The cracks became denser as the bending radius decreased. d) Crack density *ρ*, number of cracks per unit length, as a function of *ε* of different samples. The critical strain ε_c, which indicates the initiation of the microcracks, can be estimated by the interception of *ρ*-*ε* curve on *ε* axis. e) Relative

change of electrical resistance, $\Delta R/R_0$, as a function of ε. The resistance did not change until cracks formed. S is the slope of the curve after crack formation. f) Comparison of ε_c and S values amongst the four samples. g) and h) SEM images of Samples ii and iii, respectively, showing the microcracks in the Cu layer and in the interlayer. After cracks were formed on the Cu layer, the Cu layer was etched away to reveal the crack morphology, if any, in the interlayer. For Sample ii, cracks were only observed in the Cu layer. For Sample iii, cracks were observed on both the Cu layer and the Cr interlayer. The dotted circles denote the positions where crack tips on interlayer extend more than that on the Cu layer of sample iii. The schematics illustrate two possible cracking mechanisms for Samples ii and iii, respectively. The scale bars are 10 μm.

We estimated the strain tolerance of the Cu layer by observing the evolution of the microcracks and measuring the resistance change as a tensile strain is applied. We cut the samples into isosceles trapezoids, and bent the two unparallel opposite sides of the trapezoids until they contacted with each other (Figure 3b; Supplementary Figure S6). As such, a continuously varied bending radius R and tensile strain ε along the z direction, as indicated in Figure 3b, can be obtained in only one bending experiment. Microcracks were formed approximately vertical to the tensile direction (x direction), and they were denser at the positions with smaller R (Figure 3c; Supplementary Figure S7). The possible interfacial debonding between the Cu film and substrate was not observed for all the samples in the bending experiment.

Sample iv was found to be the most resilient to cracking. The crack density, ρ, expressed as the number of cracks per unit length in the tensile direction, was plotted as a function of ε (Figure 3d). ρ first increased and finally saturated as ε increased. Importantly, ρ of Sample iv was significantly smaller than those of Samples i- iii. The critical strain, ε_c, which corresponds to the minimum strain required to initiate cracking, can be estimated by extrapolating the ρ-ε curve to ρ=0 (arrow in Figure 3d)[43]. The estimated ε_c of Sample iv, ~1.6%, was also significantly larger than those of Samples i- iii, being ~0.5-0.9%. It is interesting to note that the crack behavior of Sample iv is largely improved in comparison with Sample i (i.e., crack density of sample iv is much smaller), while the calculated $\bar{\varepsilon}$ between them changes only 11% (table 1). This may be due to the complicated crack initiation and propagation of the metal thin films, which always show strong nonlinearity with respect to the applied strain[44].

The electrical stability of Sample iv also outperformed those of Samples i-iii during bending. We measured the real-time electrical response to ε and plotted the relative change of resistance, $\Delta R/R_0$, as a function of ε (Figure 3e). $\Delta R/R_0$ remained close to zero for small ε and then increased linearly when $\varepsilon > \varepsilon_c$. Therefore, the slope ($S$) of the $\Delta R/R_0$-ε curve after the crack initiation indicates the stability of electrical resistance, where smaller S means better electrical stability of a sample. S of Sample iv was much smaller than all the other samples (Figure 3f). These crack behaviors demonstrate that the nanocomposite interlayer significantly enhances the strain tolerance of the Cu film, while the PMMA or Cr interlayer does not. The experimental result is in good agreement with the predication of our principle.

Notably, although Sample iii showed smaller ρ and larger ε_c than Sample i and ii, its electrical stability was the poorest ($S\approx125$). The result is attributed to the fact that the cracks formed on the surface of Sample iii are much longer than the others (Supplementary Figure S7), which dominates the resistance change over ρ[45]. We etched away the Cu layer of cracked Samples ii and iii, and found that the generation of longer cracks was due to the lower ε_Y of the interlayer. For Sample ii, no crack was found on the PMMA interlayer (Figure 3g). In contrast, cracks with nearly the same density, shape, and position were formed on both the Cu film and the Cr interlayer of Sample iii (Figure 3h). In addition, the crack tips on the Cr interlayer extended further than on the Cu film (dotted circles in Figure 3h). Considering the fact that the Cu is more elastic than Cr, this result implies that the crack initiation first occurred on the Cr interlayer, which then induced the subsequent cracking of the Cu film at the same position. These observations indicate that the mechanism for the crack formation is controlled by the ε_Y of the interlayer. When the interlayer is more elastic than the upper film, crack initiation occurs on the upper film. When the interlayer is less elastic, cracks firstly form on the interlayer and then induce the cracking of the upper film; that is, the cracking of interlayer dominates the upper film.

To check whether our principle holds true for other conditions involving different material types, structural geometries and even loading processes, we further investigated the crack behavior of a 30-nm-thick indium tin oxide (ITO) film on 120 μm-thick polyethylene naphthalate (PEN) substrate with or without the monolayer graphene as an interlayer. Graphene is highly stiff (E~1 TPa) and of wide elastic range[46], and thus could be located at the top-right corner of Figure 2c (near the * position, carbon material). We strained the sample by the thermal loading (200 °C), and found that reticular cracks formed on the region without graphene interlayer (ITO/PEN), while the ITO film kept continuous without any cracks on the region with graphene interlayer (ITO/Graphene/PEN). This result enhances the generality of our principle (details of the experiments can be found in Materials and Methods, Supplementary Figure S8).

To demonstrate the validation of the elasto-plastic design principle on flexible electronics, we fabricated a flexible electroluminescent (EL) device consisting of bottom opaque electrode (Cu), emitter (ZnS), insulating layer (polydimethyl siloxane, PDMS), upper transparent electrode (Ag nanowires), and transparent package layer (PDMS). The device was fabricated with either a Cr or nanocomposite interlayer between the PI substrate (5 μm) and the Cu electrode (Figure 4a). The SEM image in Figure 4b shows the cross-sectional structure of the device. According to the device structure, the Cu layer shall undergo tensile strain when the device is bent, and cracks shall form on the Cu layer when the device is bent with a bending radius in the range of 0.1-0.25 mm (Figure 4b; Supplementary Note II, Supplementary Figure S9)[47]. In other words, because of the intrinsically strain-insensitive ZnS particles embedded in the PDMS matrix, the bending of the whole device cannot influence the mechanical behavior of the emitting layer, but influences the electrode (Cu layer).

As such, we intentionally bent the EL device down to *R*~0.20 mm to generate microcracks on the Cu electrode (Figure 4c). We found that the microcracks in the device using the Cr interlayer (square symbol) were generally longer, denser, and much wider than those in the device using the nanocomposite interlayer (circle symbol, Figure 4c). The microcracks increased the resistance of the electrode and the EL intensity of the devices decreased after bending. The normalized EL intensity of the device using the nanocomposite interlayer significantly outweighed that of using the Cr interlayer (Figure 4d), indicating that the introduction of an elastic and stiff nanocomposite layer enhanced the strain tolerance of the EL device. Thanks to the high stability of the Cu film with nanocomposite interlayer, the luminescent intensity of the EL device maintained nearly unchanged for 10,000 bending cycles (Figure 4e). We also patterned the Cu electrode using photolithography, and prepared an EL device with a "POLYU" logo. This EL device performed stably for various deformations, including positive bending, negative bending, twisting, and repeating grasping and releasing by hand (Figure 4f; Supplementary Movies 1 and 2).

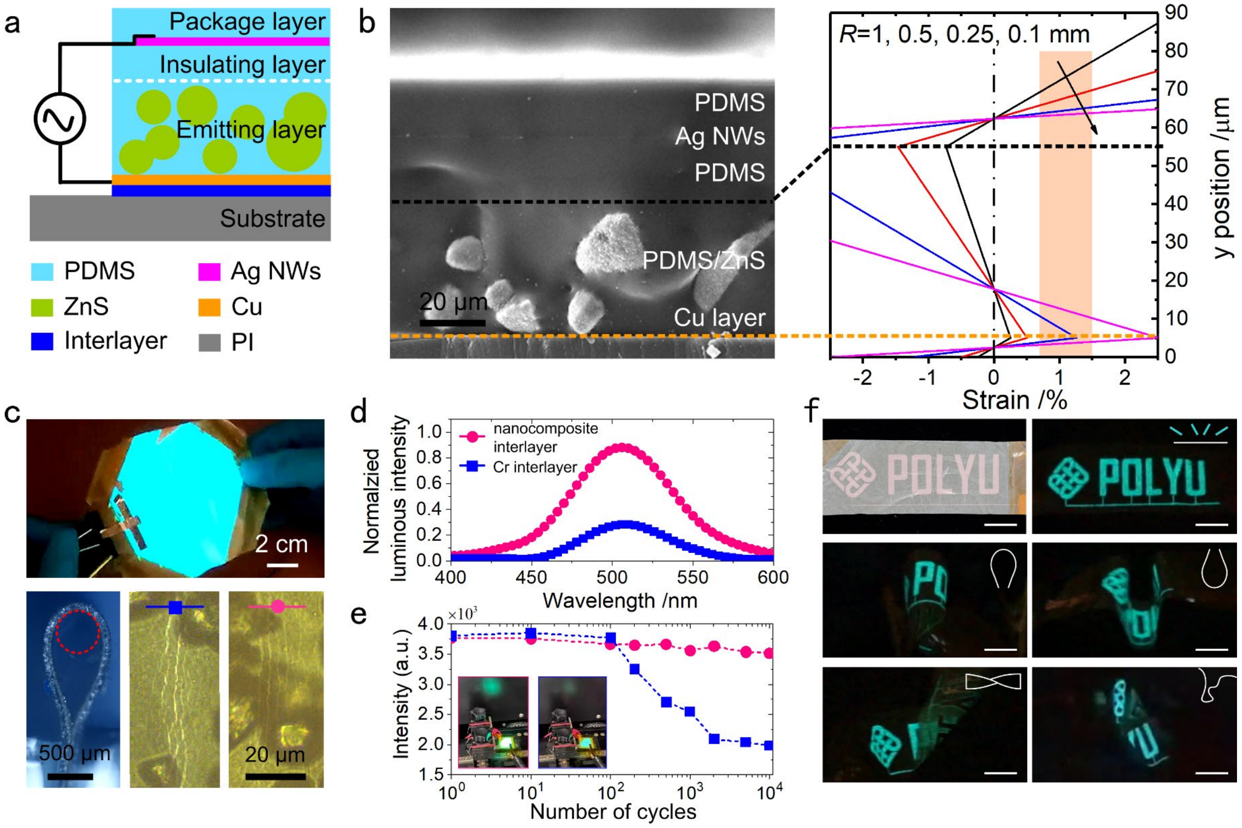

Figure 4. Proof-of-concept demonstration of the elasto-plastic strategy for highly flexible electroluminescent (EL) devices. a) Structure of an EL device, consisting of, from top to bottom, package layer, upper electrode, insulating layer, emitting layer, lower electrode, and substrate. b) SEM image of cross section of the EL device and the calculated strain distribution along thickness direction n of the device at different bending radii. As the bending radius *R* decreases to 0.1-0.25 mm, the tensile strain on the Cu layer maybe large enough to cause the crack initiation (ε~1%, highlighted region). c) Images of the EL device as an alternating voltage with of 150 Hz frequency and 125 V amplitude was applied. The device was bent at a radius of ~0.20 mm. Microcracks

formed on the device using the Cr interlayer (square symbol) is much wider and longer than those on the device with the nanocomposite interlayer (circle symbol). d) Normalized EL intensity of the devices after bending. The device using the Cr interlayer show significant drop of the EL intensity over 70%, while the one using the nanocomposite layer only drop by 10%. e) Cyclic experiment showing that the electrical stability can be enhanced by using the nanocomposite interlayer. The sample was adhered to a 20 μm thick PET substrate and the bending radius was around 2 mm. The insets show the luminescence state of the two samples after 500 bending cycles (left: nanocomposite interlayer; right: Cr interlayer). f) A patterned EL device with a “POLYU” logo using the nanocomposite interlayer, showing outstanding flexibility and stability in different deformation conditions. The scale bars are 1 cm.

Discussion

Without loss of generality, two interface-related issues need to be discussed. Firstly, the role of interfacial adhesion is not considered in our theoretical model (i.e., interfacial detachment does not take place), but indeed contributes to the deformation and crack behaviors of the film/substrate system. By performing a peeling test, Samples iv (nanocomposite interlayer) is found to possess the poorest interfacial adhesion amongst the four samples (Materials and Methods, and Supplementary Figure S10). According to the fact that a higher interfacial adhesion leads to a relieved crack of the film15, 24, one may thus envision that the crack density on Sample iv shall further decrease as its interfacial adhesion equals to that of the other samples. In other words, the difference in crack behavior between sample iii and sample iv is underestimated in our experiment due to the influence of interfacial adhesion. Similar results can be also obtained by such a comparison on the adhesion and crack behaviors between samples ii and iii, or samples iii and iv. Therefore, the difference in interfacial adhesion strongly supports our principle.

Secondly, the proposed principle is fundamentally different from the existing strain isolation theory particularly in terms of the application range and the specific content on the material selection of the interlayer. We have briefly introduced the development of the strain isolation theory as well as its simplified models, and compared them with our principle (Supplementary Note III, and Supplementary Figure S11). Generally, the strain isolation theory is applied for the design of the film/substrate system, where the middle layer is thick and soft21. For example, the usually used strain relief layer is PDMS material (1-10 MPa) with ~100 μm thickness43. However, for the opposite case where the interlayer is extremely thin and stiff, e.g., thickness from <1 μm down to several nm, and Young's modulus >10 GPa, the strain isolation theory may fail due to the numerical difficulty, while the elasto-plastic principle can address this issue. Our principle provides a guidance that can be used for the design of ultrathin interlayer with stiff material, which is widely involved in flexible electronic devices (semiconductor, ceramics, metal, and etc.), but is not covered by the strain isolation theory.

Conclusion

In summary, we have proposed a versatile principle named "elasto-plastic design of ultrathin interlayer" for enhancing the strain tolerance of flexible electronics. Our theoretical and experimental analysis have showed that an ultrathin, elastic and stiff interlayer can effectively reduce the actual strain of the upper film in a film/substrate system when it is bent. We revealed how the elasto-plastic properties of the interlayer affects the crack and electrical behavior of flexible electrodes, and demonstrated how to utilize this design principle to enhance the flexibility of electronic devices. One major advantage of using the elasto-plastic design principle is that one does not need to redesign the structure of devices or to alter the use of materials. Importantly, the elasto-plastic design principle is independent to, and compatible with existing principles considering structure thickness and interfacial bonding (Figure 1). That is, one can apply the elasto-plastic design, in additional to the existing principles, to further enhance the strain tolerance of flexible materials and devices.

Materials and Methods

FEA simulation

FEA simulations of the bending behavior of a tri-layer thin-film structure were performed on commercial software ABAQUS. The user UMAT subroutine written in FORTRAN was used to implement the elastic perfectly-plastic constitutions. The code for parametric study and the post operation were written in PYTHON. As shown in Figure 2a, the geometry was a zero-thickness 50 μm × 100 μm shell, which was meshed into 1518 S4R elements. A 150 μm × 45 μm region at the middle-left of the shell plane denoted the position where the interlayer and the upper metal film were deposited. The thicknesses of the metal, interlayer and substrate were 0.05 μm, 0.1 μm, and 5 μm, respectively. An isotropic elastic-perfectly plastic constitutive relation[48], through which the material properties could be determined by E and ε_Y, was applied to the materials. 900 times of simulations were performed to traverse all combinations of the Young's modulus (E=1-1000 GPa) and yield strain (ε_Y=0.001-0.05) of the interlayer, in which E and ε_Y were logarithmically and linearly equally spaced into 30 points, respectively. Other materials properties were E=150 GPa and ε_Y=0.01 for the upper film and E=4 GPa and ε_Y =0.1 for the substrate, which are typical values for metal film and plastic substrate, respectively. For the geometrical model of FEA (Figure 2a), symmetrical boundary condition (BC) was applied on the left short edge, while the periodic BCs were set on the two long edges. The short edge on the right was first rotated 90°, and then moved to the symmetrical axis with a displacement of 225 μm to form a curve with bending radius $R \approx 62.5$ μm. The principal strains in x direction of all the elements in the region marked with blue of the upper rigid film were averaged and referred as the tensile strain ε.

Sample preparation

Cu was electrolessly plated using the polymer-assisted metal deposition (PAMD) approach. First, a copolymer solution, poly(4-methacryloyl benzophenone-co-2-methacryloyloxy ethyltrimethylammonium chloride), [P(MBP-co-METAC)] in 2-methoxylethanol was spin-coated onto the substrate[41]. Before the PAMD approach, the substrates for Samples ii and iii were coated with 120 nm thick PMMA and 120 nm thick Cr films, respectively, while the substrates for both Samples i and iv were bare. For samples i, ii, and iii, the thickness of the copolymer in the PAMD approach was <5 nm, while that for sample iv was ~130 nm, which can be obtained by controlling the solution concentration of the copolymer and the rotational speed, i.e., 5 wt % copolymer concentration at a rotational speed of 1500 rpm for 40 s for ~130 nm thick copolymer, while 0.5 wt % at 3500 rpm for 40 s for an extremely-thin copolymer <5 nm. As such, the Cu films in the four samples were all obtained by the same deposition method, i.e., PAMD, thus posing the same material property, while the role of the copolymer in the Samples i, ii, and iii was insignificant because of its negligible geometry.

Copolymer-coated sample was thermally annealed at 120 °C for 5 min on a hotplate for the evaporation of the solvent, followed by the UV-irradiation for 5 min (365 nm, 4.8 mW cm^{-2}). Afterwards, the substrates were immersed in a 2 wt % solution of $(NH_4)_2PdCl_4$ for 3 min. Finally, the samples were rinsed with DI water, and then immersed in the Cu plating bath. The recipe of the Cu plating bath can be found in our previous publication[49, 50]. Samples for nano indentation, TEM and SEM characterization used the Si wafer as the substrate (≈500 µm thick), which was coated with a SiO_2 layer (≈1.2 µm thick) by thermal oxidization process, while samples for bending tests used the ~5 µm thick PI substrate.

The ~120 nm thick PMMA interlayer for Sample ii was prepared by spin-coating the PMMA solution (1 wt% in MMA, MW=130000, Sigma-Aldrich) at a speed of 2000 rpm for 40 s on the substrate. The ~120 nm Cr interlayer for Sample iii was obtained by the thermal evaporation technique at 2×10^{-5} chamber pressure with deposition rate of 0.05-0.08 nm s^{-1}. The PI substrate was obtained by spin-coating the pyromellitic dianhydride-oxydianiline solution (15-16 wt % in N-Methyl pyrrolidone, NMP, Sigma-Aldrich) onto a silicon wafer at a speed of 1500 rpm for 60 s, followed by the imidization with programmatic annealing process[51]. Notably, before the spin-coating of copolymer, a hydrophilic treatment was performed on the bare, PMMA-, or Cr-coated substrate by the O_2 plasma for 5 min to enhance the wettability of the copolymer on it. The free-standing PI films could be peel-offed from the Si substrate. Finally, we obtained four samples, i.e., Sample i without any interlayer as a reference, Sample ii with PMMA interlayer, Sample iii with Cr interlayer, and Sample iv with a nanocomposite interlayer (see Table 1).

Nano indentation

To obtain the material property (Young's modulus, E, and yield strain, ε_Y) of the nanocomposite generated in the PAMD process, a typical reverse approach[52] on the basis of the instrumented nano indentation experiment[53], dimension analysis[54], and iterative numerical simulation were performed (details were presented in Supplementary Note I and Supplementary Figures S4 and S5). Nanoindentation experiments were conducted at constant temperature of 20 °C on Agilent Nano Indentation system G200 using the Berkovich indenter with the dynamic contact module (DCM), by which higher resolution in both force and displacement and less sensitivity to the environment can be attained. The force-displacement curve (F-u) was obtained by setting the maximum indentation depth to 100 nm with a constant strain rate of 0.05 s^{-1} for all the samples. Continuous stiffness measurement (CSM) method with strain rate of 0.05 s^{-1} was also performed at the maximum depth. More than 15 measurements were conducted in each test. Thermal drift correction was strictly performed in each nanoindentation, which was calibrated at 10% of the maximum load during unloading process.

Image processing of microcracks

The SEM images of the microcracks were analyzed by a simple image processing for the statistic of the crack number. The image processing in order consisted of image enhancement on the neighborhood of the concerned features (cracks), bottom-hat transformation for revising the possible brightness uneven, denoising by Gaussian filter and reconstruction of a binary image by the classic OTSU thresholding algorithm[55]. The crack number was a statistic by averaging the step numbers in several row vectors in the matrix of the processed SEM binary images (Supplementary Figure S7).

Electrical response in real-time bending experiment

To measure the electrical response of the samples in real-time bending experiment, samples (i-iv) of ~5 mm in width were adhesively bonded onto a PET substrate with a total thickness of T=180 μm, and were fixed by the clamps with the initial distance L_0=1.5 cm. As one clamp moved to get closer to the other at a constant speed of v=0.05 mm s^{-1}, the sample buckled and the bending strain can be thus expressed as a function of time t, $\varepsilon = \frac{2\pi T}{L_0}\sqrt{\frac{vt}{L_0}}$ [56]. The electrical resistance of the sample was meanwhile recorded by Keithley 2400 source-meter in a 4-wire mode and at a sampling frequency of 25 Hz. Each sample was measured by 5 times, and the results were averaged. The initial electrical resistances (R_0) of samples i-iv are 21.3, 23.6, 13.5, 16.7 Ω, respectively. The R_0 of sample iv is smaller than that of samples i and ii, indicating that the Cu-polymer nanocomposite interlayer may be also conductive.

Observation of microcracks on both upper film and interlayer

In the experiment for observing the possible microcracks on interlayer, Samples ii and iii were first marked by a tinny scratch and then bent in a radius of ~0.2 mm. After capturing the cracks on the upper film (Cu) using SEM, the bent samples were immersed partially in the $FeCl_3$ solution (~0.25 mol L^{-1}), so as to etch the Cu at the center of the bending curvature and expose the interlayer.

Crack behaviors of ITO film on PEN substrate with or without graphene interlayer by thermal loading.

The monolayer CVD graphene was first released from the PMMA coated Cu foil and then transferred onto the PEN substrate (120 μm thick)[57]. The ITO solution (in water, 5% mol/L) was then spin-coated on the PEN substrate with a rotation speed of 1500 rpm for twice, resulting in a 30 nm-thick ITO film[58]. For a better understanding of the influence of the graphene interlayer on the upper rigid ITO film, the monolayer graphene only partially covered the PEN substrate. The sample was heated to 200 °C for 3 hours and then cooled to the room temperature. The thermal induced tensile strain on the upper film is thus ~2%, according to a simple formula, $\varepsilon = \Delta\alpha\Delta T$, where $\Delta\alpha$ is the difference in the coefficients of thermal expansion (CTE) between the substrate ($\alpha_{PEN} \approx 10^{-4}$/ºC[59]) and upper film ($\alpha_{ITO} \approx 5\times10^{-6}$/ºC[60]), and ΔT is the change of temperature in thermal loading ($\Delta T \approx 180$°C). The 2% strain is larger than the critical strain of the ITO film ~1%[61], leading to the initiation of the cracks. Note that, the calculated strain is the nominal strain measuring the deformation degree, but not the actual strain applied on the upper film. The latter one may be reduced due to the presence of interlayer with optimized material property. Details of the crack behaviors can be also found in Figure S8.

Fabrication of electroluminescent (EL) device

The EL device was prepared by in order spin-coating the ZnS/PDMS composite, PDMS (sylgard184, Dow Corning, USA), Ag nanowires, and PDMS on the Cu-coated PI/Si substrate to function as the emitting layer, insulating layer, upper electrode, and package layer, respectively[62]. The Ag nanowires were used as the upper electrode owing to the high transparence and stability in deformation[63]. The ZnS particles, PDMS prepolymer, and cross-linker were mixed at a mass ratio of 15: 10: 1 and then stirred for 15 min. The thickness of the emitting, insulating, and package layer is ~50 μm, ~20 μm and ~20 μm, which can be achieved at the spin-coating speed of 2000 rpm, 3000 rpm and 3000 rpm, respectively. After each spin-coating, the assembly was placed in an 80 °C oven for 2 h to cure the PDMS. To avoid the possible accumulation of the particles at the edge of the electrode due to the large temperature gradient at the early stage of the curing process, the temperature was set to increase gradually from the 25 °C to 80 °C in 30 min, and kept constant afterwards[64]. The upper electrode was achieved by spin-coating the Ag nanowire solution (5 wt % water solution) at a speed of 2000 rpm on the cured insulating PDMS layer, on which a 5 min hydrophilic treatment was in advance performed by the O_2 plasma. Finally, after the package layer was cured, the EL device was obtained by peeling off the PI film from the Si substrate carefully. To measure the EL intensity, a sinusoidal alternating voltage with a frequency of 400 Hz and an amplitude of 250 V was applied on the EL device in a dark box. The alternating voltage was generated by a waveform generator (33250A, Agilent) and a voltage amplifier (Mode 610E, Trek).

Peeling test

To exclude the possible influence of the surface roughness on the evaluation of the interfacial adhesion[65], a modified peeling test using a commercial UV-curable adhesive, NOA61, was used to compare the interfacial adhesion amongst samples i, ii, iii and iv. To conveniently count the detached area, the electrolessly-plated Cu film by PAMD method was first patterned into many POLYU logos in micro-scale by the conventional photolithography and wet etching. NOA61 was then dropped onto the patterned Cu film to cover all the logos, and a PET sheet was mounted on the top of it. 365 nm UV light with power density of 4.8 mW cm^{-2} irradiates both sides of the assembly for 30 s to cure the adhesive. Peeling test was finished by separating one sheet (PI or PET) from the other carefully. Logos partially on the PI substrate and cured adhesive denoted the undetached and detached area in the peeling test. They were captured by optical microscope (NIKON, eclipse NI-U) and were statistically counted by a simple imaging process. Details of the peeling test and adhesion characterization can be also found in Figure S11.

ASSOCIATED CONTENT

Supporting Information

The Supporting Information is available free of charge at https://

Measurement of the elasto-plastic property of Cu-polymer nanocomposite interlayer; Calculation of strain distribution along the thickness direction of the electroluminescent (EL) device; Comparison between our elasto-plastic principle and strain isolation theory; Influence of yield strain (ε_Y) and Young's modulus (E) of interlayer material on deformation behavior of upper film; Nano-indentation experiments and results; Asymmetrical bending strategy for crack observation; Graphene as an interlayer affects fracture behavior of upper ITO film; Geometrical model for tri-layer structures under bending; Peeling test for samples i-iv; and movies for EL device in various deformation modes.

AUTHOR INFORMATION

Corresponding Author

* Zijian Zheng: tczzheng@polyu.edu.hk

Author Contributions

H. H., and Z. J. Z. conceived the project; H. H., X. Y. G, Y. K. Z., Z. J. C., L. W., Z. R. W., Y. Q. Z., W. S. W., M. M. R., G. Q. L., Q. Y. H., and Z. Y. conducted the experiments; H. H. performed the FEA simulation; H. H., Z. J. Z., and Y. G. wrote the paper. All authors participated in the analysis and discussion.

Funding Sources

This work was financially supported by the RGC Senior Research Fellow Scheme (SRFS2122-5S04) and The Hong Kong Polytechnic University (1-ZVQM and 1-CD44).

ACKNOWLEDGMENT

We acknowledge the financial support from the RGC Senior Research Fellow Scheme (SRFS2122-5S04) and The Hong Kong Polytechnic University (1-ZVQM and 1-CD44).

REFERENCES

(1) Sundaram, S.; Kellnhofer, P.; Li, Y.; Zhu, J.-Y.; Torralba, A.; Matusik, W., Learning the signatures of the human grasp using a scalable tactile glove. *Nature* **2019,** *569*, 698-702.

(2) Chortos, A.; Liu, J.; Bao, Z., Pursuing prosthetic electronic skin. *Nat. Mater.* **2016,** *15*, 937-950.

(3) Zheng, Y.-Q.; Liu, Y.; Zhong, D.; Nikzad, S.; Liu, S.; Yu, Z.; Liu, D.; Wu, H.-C.; Zhu, C.; Li, J.; Tran, H.; Tok, J. B.-H.; Bao, Z., Monolithic optical microlithography of high-density elastic circuits. *Science* **2021,** *373*, 88-94.

(4) Zhang, P.; Deng, B.; Zhu, K.; Zhou, Q.; Zhang, S.; Sun, W.; Zheng, Z.; Liu, W., Wide-temperature range thermoregulating e-skin design through a hybrid structure of flexible thermoelectric devices and phase change materials heat sink. *EcoMat* **2022,** *4*, e12253.

(5) Zhang, Y.; Ng, S.-W.; Lu, X.; Zheng, Z., Solution-Processed Transparent Electrodes for Emerging Thin-Film Solar Cells. *Chem. Rev.* **2020,** *120*, 2049-2122.

(6) Luo, Y.; Wang, L.; Wei, Z.; Huang, Q.; Deng, Y.; Zheng, Z., Cracking-Controlled Slurry Coating of Mosaic Electrode for Flexible and High-Performance Lithium–Sulfur Battery. *Adv. Energy Mater.* **2022,** *n/a*, 2203621.

(7) Li, Y.; Li, N.; De Oliveira, N.; Wang, S., Implantable bioelectronics toward long-term stability and sustainability. *Matter* **2021,** *4*, 1125-1141.

(8) Cho, C.; Kang, P.; Taqieddin, A.; Jing, Y.; Yong, K.; Kim, J. M.; Haque, M. F.; Aluru, N. R.; Nam, S., Strain-resilient electrical functionality in thin-film metal electrodes using two-dimensional interlayers. *Nat. Electron.* **2021,** *4*, 126-133.

(9) Larson, C.; Peele, B.; Li, S.; Robinson, S.; Totaro, M.; Beccai, L.; Mazzolai, B.; Shepherd, R., Highly stretchable electroluminescent skin for optical signaling and tactile sensing. *Science* **2016,** *351*, 1071-1074.

(10) Shi, X.; Zuo, Y.; Zhai, P.; Shen, J.; Yang, Y.; Gao, Z.; Liao, M.; Wu, J.; Wang, J.; Xu, X.; Tong, Q.; Zhang, B.; Wang, B.; Sun, X.; Zhang, L.; Pei, Q.; Jin, D.; Chen, P.; Peng, H., Large-area display textiles integrated with functional systems. *Nature* **2021,** *591*, 240-245.

(11) Han, S. A.; Naqi, M.; Kim, S.; Kim, J. H., All-day wearable health monitoring system. *EcoMat* **2022,** *4*, e12198.

(12) Lin, R.; Kim, H.-J.; Achavananthadith, S.; Xiong, Z.; Lee, J. K. W.; Kong, Y. L.; Ho, J. S., Digitally-embroidered liquid metal electronic textiles for wearable wireless systems. *Nat. Commun.* **2022,** *13*, 2190.

(13) Zhang, Y.; Luo, Y.; Wang, L.; Ng, P. F.; Hu, H.; Chen, F.; Huang, Q.; Zheng, Z., Destructive-Treatment-Free Rapid Polymer-Assisted Metal Deposition for Versatile Electronic Textiles. *ACS Appl. Mater. Inter.* **2022,** *14*,56193-56202.

(14) Harris, K. D.; Elias, A. L.; Chung, H. J., Flexible electronics under strain: a review of mechanical characterization and durability enhancement strategies. *J. Mater. Sci.* **2016,** *51*, 2771-2805.

(15) Huang, Q.; Zheng, Z., Pathway to Developing Permeable Electronics. *ACS Nano* **2022,** *16*, 15537–15544.

(16) Wang, Z.; Li, X.; Yang, Z.; Guo, H.; Tan, Y. J.; Susanto, G. J.; Cheng, W.; Yang, W.; Tee, B. C. K., Fully transient stretchable fruit-based battery as safe and environmentally friendly power source for wearable electronics. *EcoMat* **2021,** *3*, e12073.

(17) Matsuhisa, N.; Niu, S.; O'Neill, S. J. K.; Kang, J.; Ochiai, Y.; Katsumata, T.; Wu, H.-C.; Ashizawa, M.; Wang, G.-J. N.; Zhong, D.; Wang, X.; Gong, X.; Ning, R.; Gong, H.; You, I.; Zheng, Y.; Zhang, Z.; Tok, J. B. H.; Chen, X.; Bao, Z., High-frequency and intrinsically stretchable polymer diodes. *Nature* **2021,** *600*, 246-252.

(18) Wang, D.; Zhang, Y.; Lu, X.; Ma, Z.; Xie, C.; Zheng, Z., Chemical formation of soft metal electrodes for flexible and wearable electronics. *Chem. Soc. Rev.* **2018,** *47*, 4611-4641.

(19) Xiang, Y.; Li, T.; Suo, Z.; Vlassak, J. J., High ductility of a metal film adherent on a polymer substrate. *Appl. Phys. Lett.* **2005,** *87*, 161910.

(20) Park, S.-I.; Ahn, J.-H.; Feng, X.; Wang, S.; Huang, Y.; Rogers, J. A., Theoretical and Experimental Studies of Bending of Inorganic Electronic Materials on Plastic Substrates. *Adv. Funct. Mater.* **2008,** *18*, 2673-2684.

(21) Rogers, J. A.; Someya, T.; Huang, Y., Materials and Mechanics for Stretchable Electronics. *Science* **2010,** *327*, 1603-1607.

(22) Peng, J.; Snyder, G. J., A figure of merit for flexibility. *Science* **2019,** *366*, 690-691.

(23) Fan, J. A.; Yeo, W.-H.; Su, Y.; Hattori, Y.; Lee, W.; Jung, S.-Y.; Zhang, Y.; Liu, Z.; Cheng, H.; Falgout, L.; Bajema, M.; Coleman, T.; Gregoire, D.; Larsen, R. J.; Huang, Y.; Rogers, J. A., Fractal design concepts for stretchable electronics. *Nat. Commun.* **2014,** *5*, 3266.

(24) Dai, Y.; Hu, H.; Wang, M.; Xu, J.; Wang, S., Stretchable transistors and functional circuits for human-integrated electronics. *Nat. Electron.* **2021,** *4*, 17-29.

(25) Cheng, H.; Wu, J.; Li, M.; Kim, D. H.; Kim, Y. S.; Huang, Y.; Kang, Z.; Hwang, K. C.; Rogers, J. A., An analytical model of strain isolation for stretchable and flexible electronics. *Appl. Phys. Lett.* **2011,** *98*, 061902.

(26) Wang, Z.; Lu, Q.; Xia, Y.; Feng, S.; Shi, Y.; Wang, S.; Yang, X.; Zhao, Y.; Sun, F.; Li, T.; Zhang, T., Stable epidermal electronic device with strain isolation induced by in situ Joule heating. *Microsyst. Nanoeng.* **2021,** *7*, 56.

(27) Wang, W.; Wang, S.; Rastak, R.; Ochiai, Y.; Niu, S.; Jiang, Y.; Arunachala, P. K.; Zheng, Y.; Xu, J.; Matsuhisa, N.; Yan, X.; Kwon, S.-K.; Miyakawa, M.; Zhang, Z.; Ning, R.; Foudeh, A. M.; Yun, Y.; Linder, C.; Tok, J. B. H.; Bao, Z., Strain-insensitive intrinsically stretchable transistors and circuits. *Nat. Electron.* **2021,** *4*, 143-150.

(28) Lu, N.; Wang, X.; Suo, Z.; Vlassak, J., Metal films on polymer substrates stretched beyond 50%. *Appl. Phys. Lett.* **2007,** *91*, 221909.

(29) Li, T.; Huang, Z. Y.; Xi, Z. C.; Lacour, S. P.; Wagner, S.; Suo, Z., Delocalizing strain in a thin metal film on a polymer substrate. *Mech. Mater.* **2005,** *37*, 261-273.

(30) Hamdi, M.; Poulis, J. A., Effect of UV/ozone treatment on the wettability and adhesion of polymeric systems. *J. Adhes.* **2021,** *97*, 651-671.

(31) Lee, C.-C.; Shih, R.-C.; Huang, P.-C.; Tseng, S.-F., Adhesion enhancement of conductive graphene/PI substrates through a vacuum plasma system. *Surf. Coat. Technol.* **2020,** *388*, 125601.

(32) Cai, F.; Zhang, J.; Wang, J.; Zheng, J.; Wang, Q.; Zhang, S., Improved adhesion and erosion wear performance of CrSiN/Cr multi-layer coatings on Ti alloy by inserting ductile Cr layers. *Tribol. Int.* **2021,** *153*, 106657.

(33) Kim, J. J.; Wang, Y.; Wang, H.; Lee, S.; Yokota, T.; Someya, T., Skin Electronics: Next-Generation Device Platform for Virtual and Augmented Reality. *Adv. Funct. Mater.* **2021,** *31*, 2009602.

(34) Briscoe, B.; Fiori, L.; Pelillo, E., Nano-indentation of polymeric surfaces. *J. Phys. D: Appl. Phys.* **1998,** *31*, 2395.

(35) Li, H.; Chen, J.; Chen, Q.; Liu, M., Determining the constitutive behavior of nonlinear visco-elastic-plastic PMMA thin films using nanoindentation and finite element simulation. *Mater. Des.* **2021,** *197*, 109239.

(36) Seltzer, R.; Cisilino, A. P.; Frontini, P. M.; Mai, Y.-W., Determination of the Drucker–Prager parameters of polymers exhibiting pressure-sensitive plastic behaviour by depth-sensing indentation. *Int. J. Mech. Sci.* **2011,** *53*, 471-478.

(37) Noii, N.; Aghayan, I., Characterization of elastic-plastic coated material properties by indentation techniques using optimisation algorithms and finite element analysis. *Int. J. Mech. Sci.* **2019,** *152*, 465-480.

(38) Kataria, S.; Goyal, S.; Dash, S.; Tyagi, A. K., Nanomechanical characterization of thermally evaporated Cr thin films — FE analysis of the substrate effect. *Thin Solid Films* **2010,** *519*, 312-318.

(39) Ding, Y.; Zhang, F.; Yan, S.; Li, H.; He, J.; Yin, F., Microstructure, Micro-Indentation, and Scratch Behavior of Cr Films Prepared on Al alloys by Using Magnetron Sputtering. *Metals* **2019,** *9*, 1330.

(40) Li, P.; Zhang, Y.; Zheng, Z., Polymer-Assisted Metal Deposition (PAMD) for Flexible and Wearable Electronics: Principle, Materials, Printing, and Devices. *Adv. Mater.* **2019,** *31*, 1902987.

(41) Yu, Y.; Xiao, X.; Zhang, Y.; Li, K.; Yan, C.; Wei, X.; Chen, L.; Zhen, H.; Zhou, H.; Zhang, S.; Zheng, Z., Photoreactive and Metal-Platable Copolymer Inks for High-Throughput,

Room-Temperature Printing of Flexible Metal Electrodes for Thin-Film Electronics. *Adv. Mater.* **2016,** *28*, 4926-34.

(42) Ghosh, S., Electroless copper deposition: A critical review. *Thin Solid Films* **2019,** *669*, 641-658.

(43) Zhu, X. F.; Zhang, B.; Gao, J.; Zhang, G. P., Evaluation of the crack-initiation strain of a Cu–Ni multilayer on a flexible substrate. *Scripta Mater.* **2009,** *60*, 178-181.

(44) Li, J.; Li, C.; Li, L.; Wang, Q.; Wang, Z.; Wang, S.; Sun, C., Study on fracture behavior in stiff-thin-film-on-soft-substrate structures under biaxial stress state. *Int. J. Solids Struct.* **2021,** *219-220*, 51-62.

(45) Glushko, O.; Kraker, P.; Cordill, M. J., Explicit relationship between electrical and topological degradation of polymer-supported metal films subjected to mechanical loading. *Appl. Phys. Lett.* **2017,** *110*, 191904.

(46) Cao, K.; Feng, S.; Han, Y.; Gao, L.; Hue Ly, T.; Xu, Z.; Lu, Y., Elastic straining of free-standing monolayer graphene. *Nat. Commun.* **2020,** *11*, 284.

(47) Shi, Y.; Rogers, J. A.; Gao, C.; Huang, Y., Multiple Neutral Axes in Bending of a Multiple-Layer Beam With Extremely Different Elastic Properties. *J. Appl. Mech.* **2014,** *81*, 114501.

(48) Chatterjee, A.; Polycarpou, A. A.; Abelson, J. R.; Bellon, P., Nanoscratch study of hard HfB2 thin films using experimental and finite element techniques. *Wear* **2010,** *268*, 677-685.

(49) Gao, Y.; Hu, H.; Chang, J.; Huang, Q.; Zhuang, Q.; Li, P.; Zheng, Z., Realizing High-Energy and Stable Wire-Type Batteries with Flexible Lithium–Metal Composite Yarns. *Adv. Energy Mater.* **2021,** *11*, 2101809.

(50) Zhang, Y.; Wang, W.; Wang, L.; Guo, Q.; Hu, H.; Xie, C.; Shang, J.; Xu, J.; Zhang, Y.; Zheng, Z., Inverse Opaline Metallic Membrane Addresses the Tradeoff Between Volumetric Capacitance and Areal Capacitance of Supercapacitor. *Adv. Energy Mater.* **2022,** *12*, 2102802.

(51) Mao, S.; Li, J.; Guo, A.; Zhao, T.; Zhang, J., An Active Multielectrode Array for Collecting Surface Electromyogram Signals Using a-IGZO TFT Technology on Polyimide Substrate. *IEEE Trans. Electron. Dev.* **2020,** *67*, 1613-1618.

(52) Zhao, M.; Chen, X.; Xiang, Y.; Vlassak, J. J.; Lee, D.; Ogasawara, N.; Chiba, N.; Gan, Y. X., Measuring elastoplastic properties of thin films on an elastic substrate using sharp indentation. *Acta Mater.* **2007,** *55*, 6260-6274.

(53) Ma, Y.; Huang, X.; Hang, W.; Liu, M.; Song, Y.; Yuan, J.; Zhang, T., Nanoindentation size effect on stochastic behavior of incipient plasticity in a LiTaO3 single crystal. *Eng. Fract. Mech.* **2020,** *226*, 106877.

(54) Long, X.; Jia, Q. P.; Li, Z.; Wen, S. X., Reverse analysis of constitutive properties of sintered silver particles from nanoindentations. *Int. J. Solids Struct.* **2020,** *191-192*, 351-362.

(55) Talab, A. M. A.; Huang, Z.; Xi, F.; HaiMing, L., Detection crack in image using Otsu method and multiple filtering in image processing techniques. *Optik* **2016,** *127*, 1030-1033.

(56) Song, J.; Huang, Y.; Xiao, J.; Wang, S.; Hwang, K. C.; Ko, H. C.; Kim, D. H.; Stoykovich, M. P.; Rogers, J. A., Mechanics of noncoplanar mesh design for stretchable electronic circuits. *J. Appl. Phys.* **2009,** *105*, 123516.

(57) Wang, Z.; Hao, Z.; Wang, X.; Huang, C.; Lin, Q.; Zhao, X.; Pan, Y., A Flexible and Regenerative Aptameric Graphene–Nafion Biosensor for Cytokine Storm Biomarker Monitoring in Undiluted Biofluids toward Wearable Applications. *Adv. Funct. Mater.* **2021,** *31*, 2005958.

(58) Kim, M.-G.; Kanatzidis, M. G.; Facchetti, A.; Marks, T. J., Low-temperature fabrication of high-performance metal oxide thin-film electronics via combustion processing. *Nat. Mater.* **2011,** *10*, 382-388.

(59) Zoo, Y.; Adams, D.; Mayer, J. W.; Alford, T. L., Investigation of coefficient of thermal expansion of silver thin film on different substrates using X-ray diffraction. *Thin Solid Films* **2006,** *513*, 170-174.

(60) Tien, C.-L.; Lin, T.-W., Out-of-Plane Thermal Expansion Coefficient and Biaxial Young's Modulus of Sputtered ITO Thin Films. *Coatings* **2021,** *11*, 153.

(61) Peng, C.; Jia, Z.; Bianculli, D.; Li, T.; Lou, J., In situ electro-mechanical experiments and mechanics modeling of tensile cracking in indium tin oxide thin films on polyimide substrates. *J. Appl. Phys.* **2011,** *109*, 103530.

(62) Nie, B.; Wang, C.; Li, X.; Tian, H.; Chen, X.; Liu, G.; Qiu, Y.; Shao, J., High-Performance Transparent and Conductive Films with Fully Enclosed Metal Mesh. *ACS Appl. Mater. Interfaces* **2021,** *13*, 40806-40816.

(63) Wang, C.; Shao, J.; Tian, H.; Li, X., Protective integrated transparent conductive film with high mechanical stability and uniform electric-field distribution. *Nanotechnology* **2019,** *30*, 185303.

(64) Ding, X.; Shao, C.; Peng, Z.; Yu, B.; Li, Z.; Yang, S., Study on Convective Flow Behaviors of Phosphor Particles During Curing Process of Silicone and the Influences on the Optical Performance of White LEDs. *IEEE Trans. Electron. Dev.* **2021,** *68*, 2778-2784.

(65) Hu, H.; Zhao, S.; Wang, W.; Zhang, Y.; Fu, Y.; Zheng, Z., Prediction of adhesion between randomly rough surfaces by order statistics. *Appl. Phys. Lett.* **2021,** *119*, 071603.